Aeromechanical optimization of first row compressor test stand blades using a hybrid machine learning model of genetic algorithm, artificial neural networks and design of experiments

Mohammad Ghalandari, Alireza Ziamolki, Amir Mosavi, Shahaboddin Shamshirband, Kwok-Wing Chau & Saeed Bornassi

Taylor & Francis
Taylor & Francis Group

∂ OPEN ACCESS | Check for updates

Aeromechanical optimization of first row compressor test stand blades using a hybrid machine learning model of genetic algorithm, artificial neural networks and design of experiments

Mohammad Ghalandari[a], Alireza Ziamolki[a], Amir Mosavi[b,c], Shahaboddin Shamshirband [d,e], Kwok-Wing Chau[f] and Saeed Bornassi[a]

[a]Research and Development Department, MAPNA Turbine Engineering and Manufacturing Company (TUGA), Karaj, Iran; [b]School of the Built Environment, Oxford Brookes University, Oxford, UK; [c]Kando Kalman Faculty of Electrical Engineering, Institute of Automation, Obuda University, Budapest, Hungary; [d]Department for Management of Science and Technology Development, Ton Duc Thang University, Ho Chi Minh City, Vietnam; [e]Faculty of Information Technology, Ton Duc Thang University, Ho Chi Minh City, Vietnam; [f]Department of Civil and Environmental Engineering, Hong Kong Polytechnic University, Hong Kong, People's Republic of China

ABSTRACT

In this paper, optimization of the first blade of a new test rig is pursued using a hybrid model comprising the genetic algorithm, artificial neural networks and design of experiments. Blade tuning is conducted using three-dimensional geometric parameters. Taper and sweep angle play important roles in this optimization process. Compressor characteristics involving mass flow and efficiency, and stress and eigenfrequencies of the blades are the main objectives of the evaluation. Owing to the design of blade attachments and their dynamic isolation from the disk, the vibrational behavior of the one blade is tuned based on the self-excited and forced vibration phenomenon. Using a semi-analytical MATLAB code instability, the conditions are satisfied. The code uses Whitehead's theory and force response theory to predict classical and stall flutter speeds. Forced vibrational instability is controlled using Campbell's theory. The aerodynamics of the new blade geometry is determined using multistage computational fluid dynamics simulation. The numerical results show increasing performance near the surge line and improvement in the working interval along with a 4% increase in mass flow. From the vibrational point of view, the reduced frequency increases by at least 5% in both stall and classical regions, and force response constraints are satisfied.

1. Introduction

Aeromechanical considerations are the major issue in developing advanced turbomachinery blades. In addition to strength criteria, the main critical aeroelastic problems, involving flutter, forced response and asynchronous vibration, can affect the design criteria of the blades. Forced response and asynchronous vibrations originate from aerodynamic sources, whereas flutter instability is caused by the interaction of the motion of the blades and the aerodynamic forces. All these phenomena, and especially flutter, which has a limit-cycle oscillation besides the oscillatory aerodynamic loading, are arguably the most important factors in the design of durable blades. The stress induced by these excitations should be confined to the minimum possible level even under resonance conditions, where the amplitude of the vibration can increase significantly and is usually the main cause of high cycle fatigue failure.

The flutter phenomenon as a root cause of failure in turbomachinery blades is still under investigation by many researchers. Early studies on flutter speed prediction in turbomachinery and evaluation of its consequences on blade failure were conducted by Whitehead (1965, 1966, 1973). His presented method was based on the simple aeroelastic model for cascades which were exposed to a subsonic airflow. The vortex panel theory and non-penetrating flow boundary conditions support the analytical solution of lift and moment of the cascade in flexural and torsional oscillating modes. The theory has been established based on Theodorsen and Mutchler's (1935) aerodynamic model, which predicts classical flutter for a single oscillating airfoil. The incompressibility of inviscid flow and the low angle of attack of flat airfoils are other fundamental assumptions of the model. Later, Mikolajczak, Arnoldi, Snyder, and Stargardter (1975), Lubomski (1980), Kielb and Kaza (1983)

and Srinivasan (1997) extended the Whitehead theory and suggested different limits for classical and stall flutter instability.

From a design point of view, shrouds, clappers and dampers are coupling components that are commonly applied to reduce or postpone the disturbance effects of these dynamic phenomena. In addition, the elastic axis

Figure 1. Newly presented compressor test stand.

position of the blades can influence aerostructural problems. Therefore, geometric parameters such as the sweep angle and taper ratio can play a positive role in aerostructural modifications of the blades (Pathak, Kushari, & Venkatesan, 2008).

Nowadays, the blade shape is often designed using an optimization tool. Multidisciplinary design optimization (MDO) is a powerful method commonly applied to the design and optimization of turbomachinery components (Ashihara, Goto, Guo, & Okamoto, 2004; Deng, Shao, Fu, Luan, & Feng, 2018; Iwaniuk, Wiśniowski, & Żółtak, 2016; Xiaodong & Xiuli, 2015; Zhang, Gou, Li, Wang, & Yue, 2016). Demeulenaere, Ligout, and Hirsch (2004) took advantage of the MDO approach to create the optimum shape of the disk and blade turbine components. Shen, Cao, and Yang (2009), using MDO and thermoelastic–plastic analysis, presented an algorithm to extract the shape of the blades and disk. Luo, Song, Li, and Feng (2009) introduced a simplified three-dimensional (3D) transonic blade based on MDO. The finite element method (FEM) and computational fluid dynamics (CFD) (Faizollahzadeh Ardabili et al., 2018) are robust and efficient methods which have facilitated the design
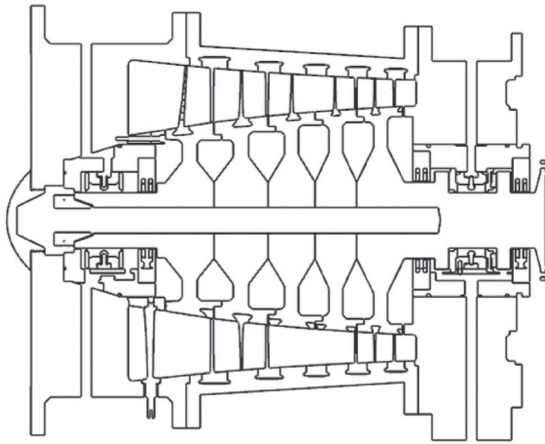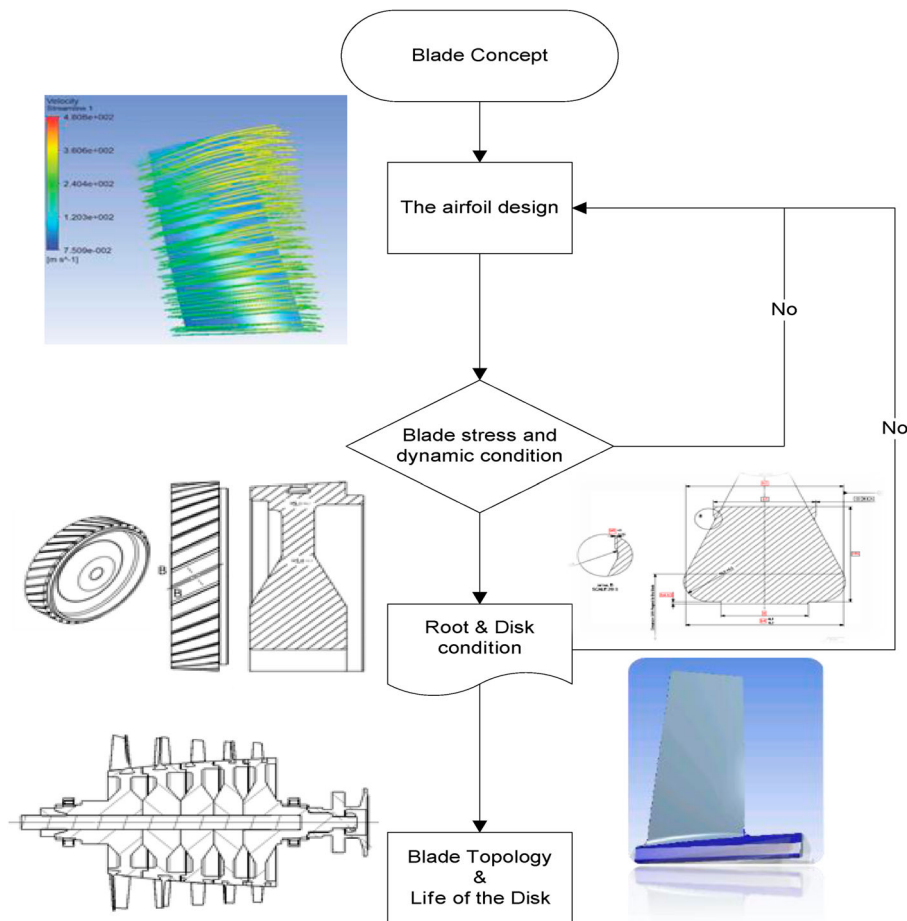

Figure 2. Classical design flow of the blade.

process (Ghalandari, Mirzadeh Koohshahi, Mohamadian, Shamshirband, & Chau, 2019).

In this paper, optimization of the first rotary blades in a new axial compressor test stand (Figure 1) with a common design flow consideration (Figure 2) is presented. The compressor has five stages, each with 3.5 pressure and 9 temperature ratios, and operates in the speed range of 9500–16,500 rpm.

Because of the occurrence of flutter of the main blades in the first stage, which is a challenging part of this project, aeromechanical assessments in both stall and classical regions are performed; and using the MDO technique, CFD and FEM, the best shape of the blades is extracted. Taper ratio and sweep are the main geometric parameters in the presented optimization process, which is performed on the US National Advisory Committee for Aeronautics (NACA) 65 basic airfoil. Therefore, our structural considerations were flutter speed prevention and setting a reasonable margin for forced response and steady-state stress. The aerodynamic objectives were to optimize the characteristics of the compressor and increase the performance of each stage.

2. Case study

Sweep angle, which is created by dislocation of the cross-section along the chord of the airfoil, plays an important role in the performance of axial turbomachinery. In general, the 3D influences of the blade with a sweep effect are enhancements in the efficiency and range of the operation. Aerodynamic studies have shown that this parameter can increase the pressure ratio value, limit the secondary loss effects, decrease the loading near the leading edge and reduce blockage in the tip area of the blades. The sweep angle can also change the shockwave structure and improve the loss effects in transonic systems. The advantages of the forward swept blade are highlighted, so that it has direct effects on aerodynamic parameters involving leading edge loading, incidence angle effects and leakage (Pathak et al., 2008). From the mechanical point of view, sweep angle can also change the elastic axis position and alter the dynamic behavior. Investigation of the presented main blades with 80 mm length (Figure 3) and material of 26NiCrMov145 (Table 1) shows that the sweep parameter has an effect of about 1.5%, especially on the second mode (first torsional mode) (Table 2); aeroelastic failure of turbomachinery blades, as in our test case, usually occurs in this mode.

Taper parameters such as sweep angle have a great impact on performance and other aerodynamic characteristics. Taper parameters can increase the frequency of the blades (Kaza & Kielb, 1985) but have negative effects on the compressor characteristics (Figure 4).
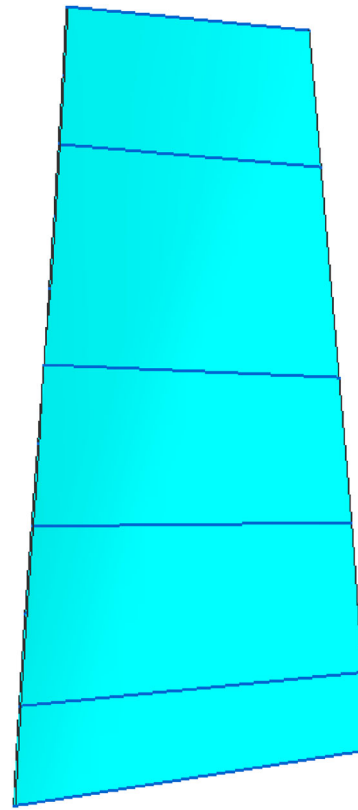

Figure 3. Main blade geometry.

Table 1. Cord length and twist angle distribution of the NACA 65 airfoil along the main blade span.

Blade span (r/R)	Chord (C/R)	Stagger angle (degrees)
0.12	0.18	28.51
0.36	0.18	33.49
0.60	0.179	39
0.84	0.179	48
1	0.179	50

Table 2. Sweep effects on the second and third mode frequencies.

Mode	Main blade frequency (Hz)	Sweep backward blade frequency (Hz)	Sweep forward blade frequency (Hz)
First torsion	1405.2	1427.3	1381.3

3. Description of optimization process

MDO (Shen et al., 2009), as a relatively new conventional method, and other in-house modules can produce a axial turbomachinery blades with good performance and an acceptable range of mechanical criteria. By combining a genetic algorithm (GA) and an artificial neural network (ANN) with low cost and high-speed calculations, based on the MDO method, the design process of the main blade is accomplished. These design activities
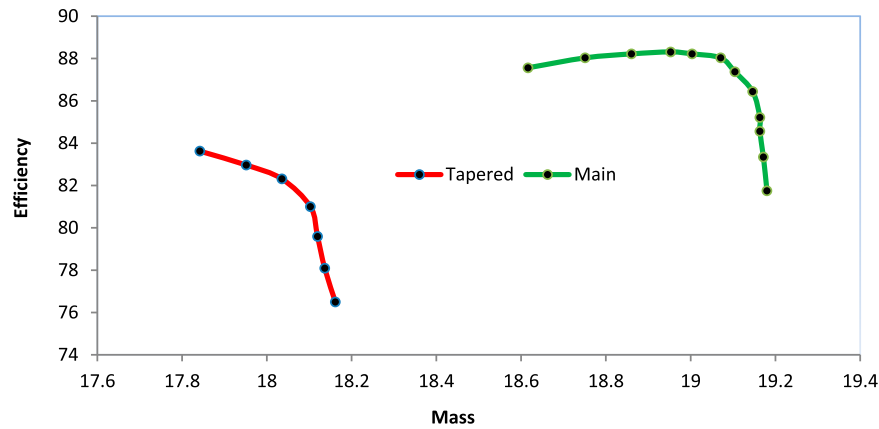
Figure 4. Aerodynamic effects of tapering.

include adaptive geometric parameterization, an evolutionary optimization algorithm and a popular surrogate model using highly efficient 3D aeromechanical software. This process starts with the creation of a database based on the design of experiments (DOE) method, main blade specifications and ANN models. Bezier control points affect the distributions of thickness and sweep angle for the generation of new geometries. By generating a database, the interactions and accuracy of the selected bounds for each variable are evaluated.

Using the trained ANN, the results of the new geometry are generated, some special estimations of the ANN are numerically modeled and the target results are added to the database. This procedure is conducted until the results of the ANN converge with the numerical results. Finally, design software is used to assess the objective function under the given boundary conditions with regard to mechanical constraints.

4. Geometric parameterization

The geometry is parameterized with a conventional Bezier method using an in-house tool. The geometry is defined by a certain number of parameterized airfoil sections with a distribution of camber lines and thicknesses. Each two-dimensional (2D) section can be parameterized by 15 Bezier control points, five control points for the camber line and 10 control points for the thickness distribution. The definition of changes in the control points depends on the geometric constraints and properties of the boundary conditions; in this design, some control points in the blade's leading and trailing edges are fixed locally. The variation in the control points of each section depend on the other sections, and this can reduce the disturbances occurring on the generated blade's surface. The stacking line is parameterized by five control points; this can enable the sweep angle of the blade geometry to
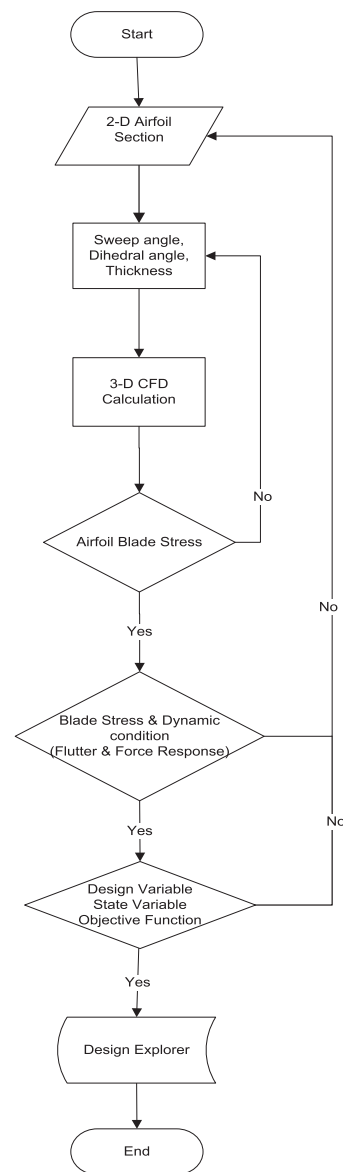

Figure 5. Optimized design flow of the blade. CFD = computational fluid dynamics.

be changed. In the spanwise direction, the definition of movable control points differs. The selection of appropriate control points and their margin of variation, from minimum to maximum values, is very important because this selection should be made so that the geometry can obtain the best position with the least amount of dissonant geometry. The selection of inappropriate control points with unsuitable margins can lead to more computational time being required, with errors in the design procedure.

5. Calculation

Generated geometries are evaluated on design and off-design operating points based on the sensed boundary conditions. Geometric parameters, consisting of the stack-line position defining the sweep angle and thickness in UG software, are considered as design variables to maximize the stage characteristics. Aeromechanical considerations also play a key role in the design of blades. Vibratory constraints are introduced based on the flutter and forced response criteria. The margins of the first three frequencies of the blade are set to be at least 3–5% in the lower and upper bands of the Campbell diagram. This condition generate forbidden ranges for speed: 9000–10,000, 10,000–11,000, . . . 16,000–17,000. In addition, the flutter criterion should be satisfied in both operational (classical theory) and stall regions based on the recommended reduced frequencies (Lubomski, 1980). Thus, using the above-mentioned parameters, the objective function (OF) created by mass flow and efficiency can be written as:

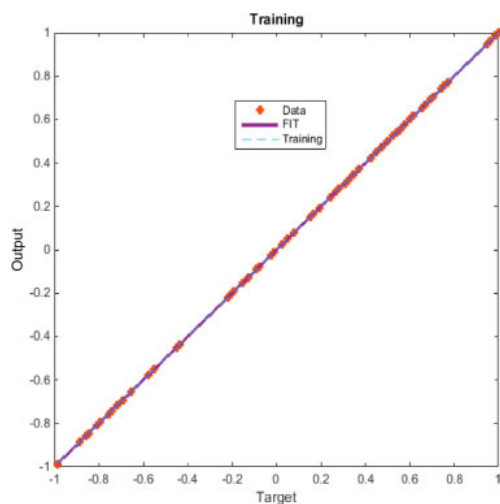$$OF = \eth_1 \frac{\eta_o}{\eta_b} + \eth_2 \frac{\tau_o}{\tau_b} \tag{1}$$

where $\eth_k$ is defined as a weighting coefficient with equal values that indicate the importance of each parameter, η_o/η_b is the efficiency ratio, and τ_o/τ_b is the mass ratio.

The optimization process is conducted based on the flowchart in Figure 5. Owing to the proper range of the main blade efficiency (η_b) in both design and off-design working intervals, the aerodynamic constraints are adjusted to have a much higher weighting value on
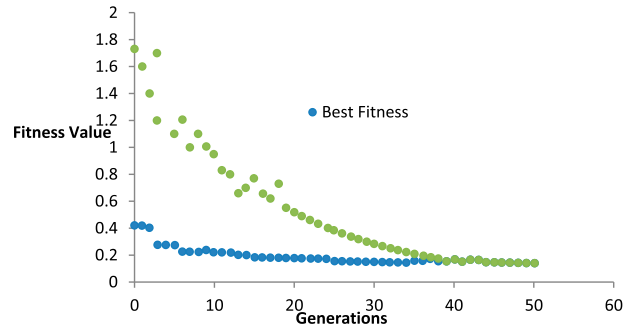

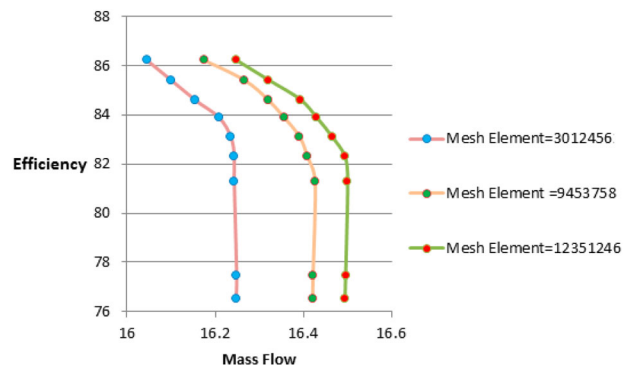**Figure 7.** Fitness value versus number of generations.

Figure 8. Computational fluid dynamics (CFD) mesh study.

Figure 6. Network training and validation of efficiency calculation.

mass flow. The idea takes advantage of rough meta-models. The ANN is trained using 3D CFD analyses, which were created by a DOE technique. The type of ANN employed in this study is a feed-forward back-propagation network with 15 hidden layers and one output neuron. Based on experience, the acceptable range of the geometric parameters in training the network is set to be within a 5% deviation of the main blade parameters. The optimization cycle is started with the presented approximated function values (Equation 1) by the ANN,

and the GA is used to find the optimized point of the approximated function and validated with 3D CFD solutions to update the ANN model.

6. Results and discussion

The results of the optimization procedure are presented in this section. Based on the DOE matrix selected here, 64 experiments were performed, of the Latin hypercube type. In the first step, based on 70% of the experiments,
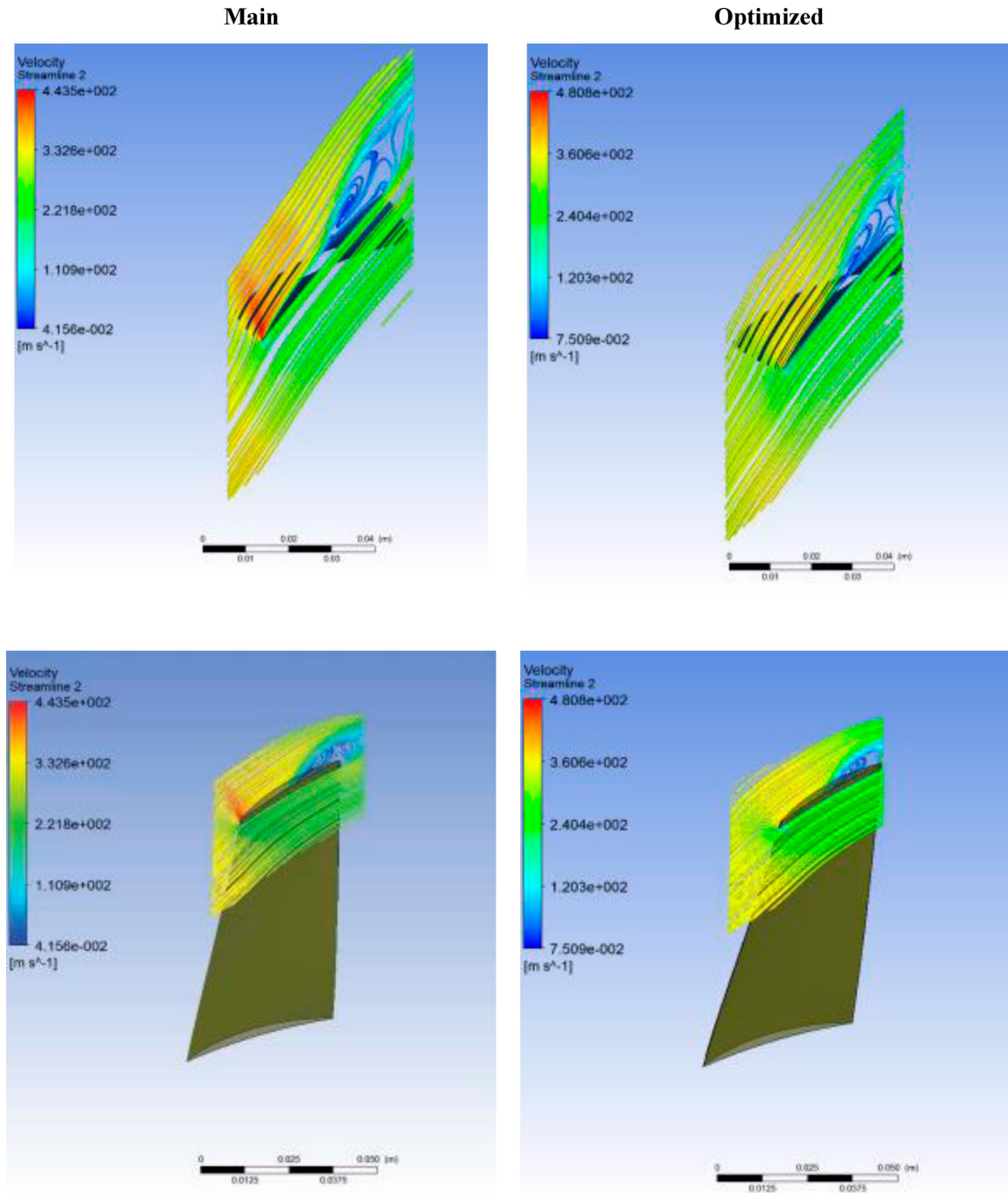

Figure 9. Aerodynamic comparison of the main and optimized blades.

the neural network was trained; then, the remaining 30% of the data was evaluated by the validation of the network. The ANN results for efficiency show 99.9% precision in the training procedure and 0.09% deviations in data validations of the ANN (Figure 6).

In the optimization process, each time the GA is executed and the network is used as a tool for evaluating the produced geometry, two elite geometries are compared to 3D solutions to estimate the accuracy of the network results, and the results of the 3D solution and the network estimation are compared. In the event of an error of more than 0.5%, the 3D solution results are added to the database and the network is retrained. After reducing the error to less than 0.5%, the 3D calculations
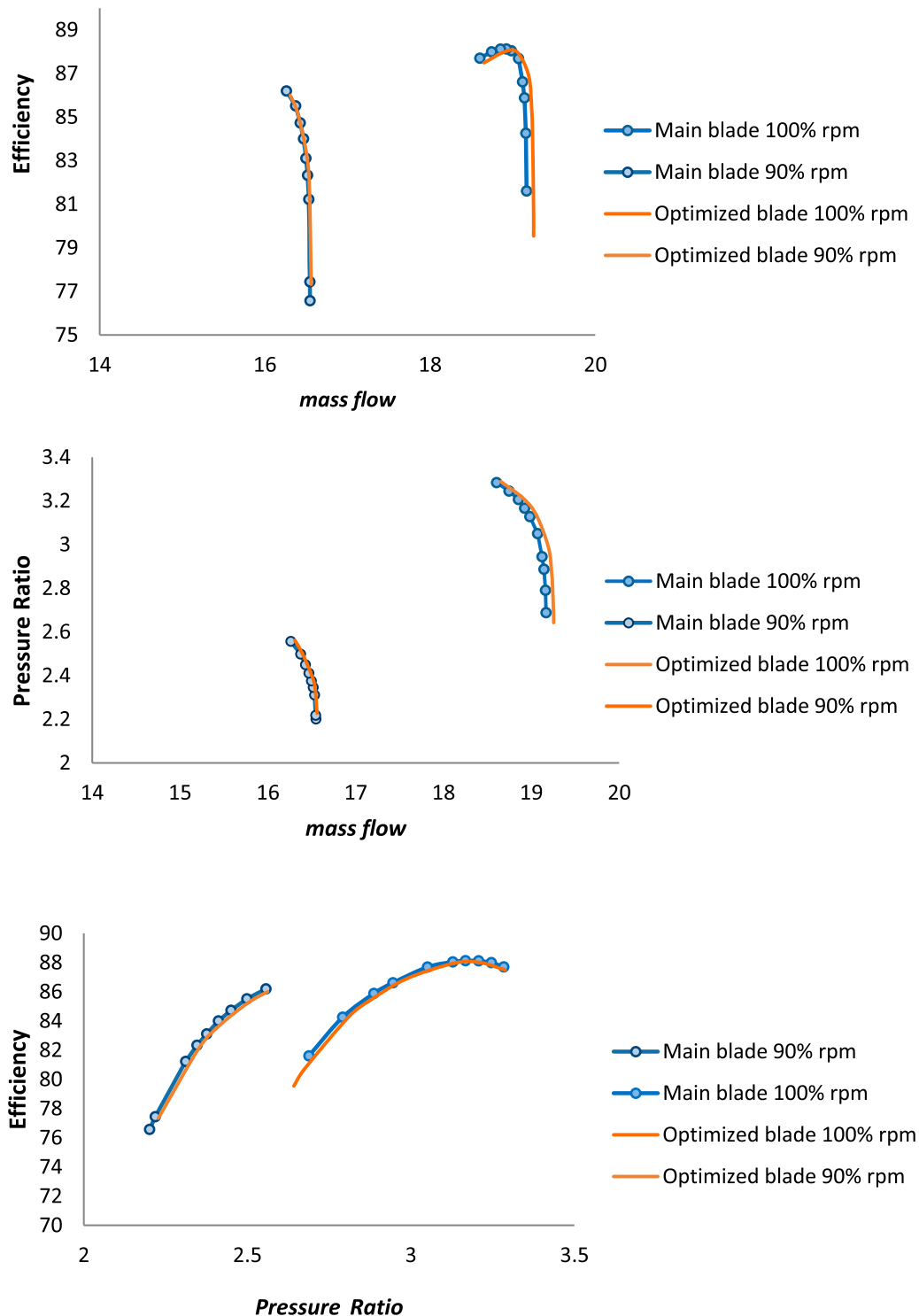

Figure 10. Comparison of main and optimized blade characteristics.

are completely eliminated from the optimization cycle and the algorithm continues with optimization using the neural network only. Optimization is followed up by a 50-generation GA, which exists in each generation of 100 members (Figure 7). The fitness value started at nearly 2 and reached a value less than 0.2. The results are assessed by CFD and FEM in the optimization loop and compared with the main blade characteristics to obtain the best geometry of the blade.

6.1. Aerodynamic analysis

The aerodynamic study takes advantage of the CFD analysis and is based on the loosely coupled method. Specific aerodynamic loading of the blades is calculated by definition of the wall boundary conditions and fluid domain analysis. The boundary condition consists of the inlet and outlet boundaries and cyclic symmetry conditions. CFD calculations are conducted based on the $K - \varepsilon$ model and the efficiency value is controlled within $\pm 0.5\%$ of the main working interval. A mesh study is conducted to prove the adequacy of convergence values for the CFD calculation (Figure 8).

Table 3. Structural mesh study.

Mesh	FEM calculation	
	Mesh element	Mode 1 (Hz)
1	10,000	369.5
2	40,000	354.1
3	90,000	353.2

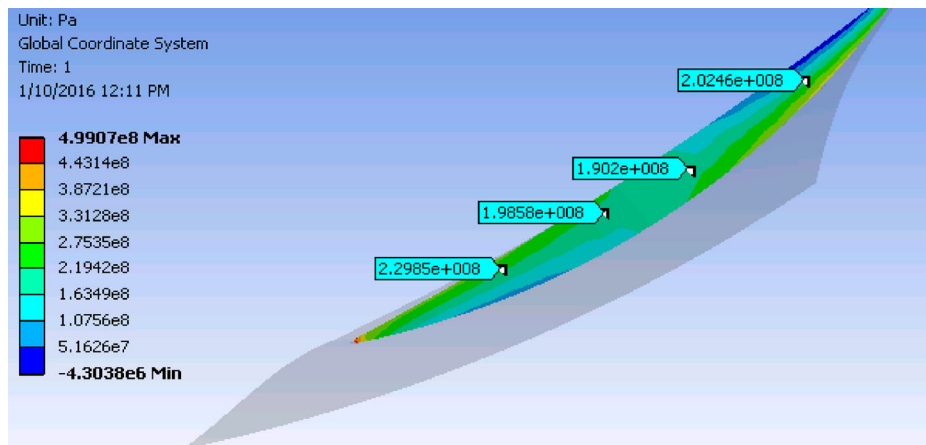Note: FEM = finite element method.

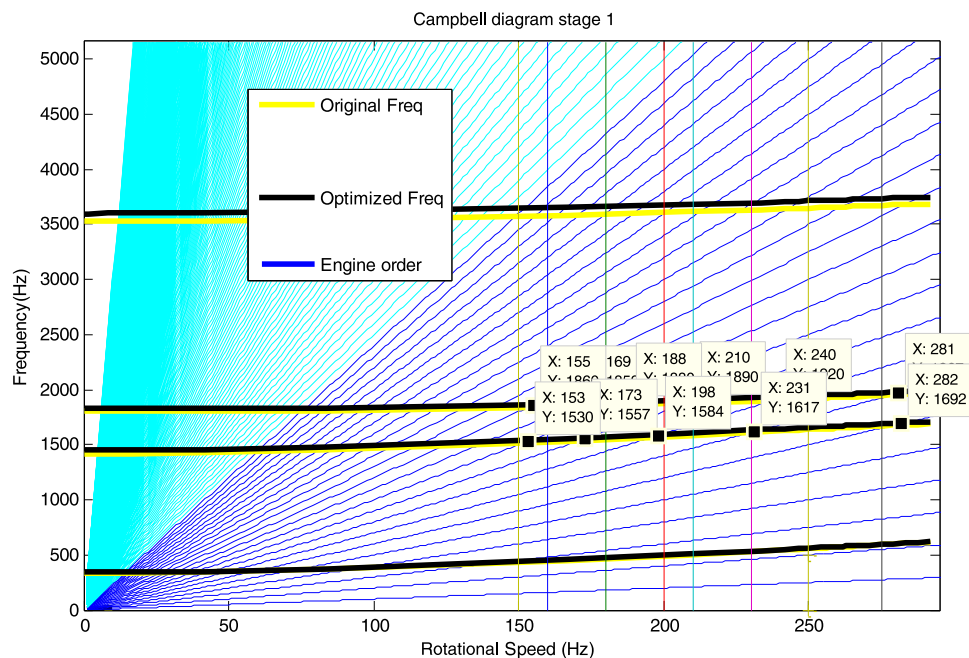
Figure 11. Blade root and hub stress level.

Figure 12. Campbell diagram of the blade.

Figure 9 illustrates the velocity domain around the airfoil in the tip of the blade. Based on the CFD calculation, separate construction of the optimized blade gives a smaller area than the main blade.

From the results (Figure 10), an increased mass flow value of at least 4% in both design and off-design operational conditions is highlighted. In addition, the efficiency values show a 0.12% decrease in design and 0.08% increase in off-design compared with the main blade.

6.2. Structural analysis

Static and dynamic structural analyses were conducted using prestress modal analysis in the optimization framework (Shen et al., 2009). Mesh convergence values with the SOLID186 element for FEM structural analysis of the fundamental frequency used 40,000 element values (Table 3).

Based on the safe-life design theory, a safety factor equal to 1.5 versus the strength of the blades is considered. Here, the condition of maximum stress, which generally occurs in the hub area, does not represent a limiting factor in the optimization procedure because

Table 4. Optimized and main blade frequencies at 9000 rpm.

	Main blade			Optimized blade		
	Mode 1	Mode 2	Mode 3	Mode 1	Mode 2	Mode 3
Frequency (Hz)	412.2	1513.2	1841.4	438.5	1543.1	1868.6

Table 5. Stall flutter investigation.

Reduced frequency	Mode	
0.527	1	Main blade
1.5	2	
0.54	1	Optimized blade
1.56	2	

the maximum von Mises stress is always below 500 MPa (Figure 11).

An appropriate interval speed to satisfy the forced response, as constructed by the Campbell diagram, needs to be checked based on all the criteria mentioned in the set-up phase. As illustrated in Figure 12, the interval speed is increased. The amount of increase for the first three frequency modes is about 1.9% (Table 4). Therefore, the forced response investigation prove that the optimized blade is free from resonance conditions in the mentioned operating range, with regard to American Petroleum Institute (API) recommendations (Yaozeng, Wenxiang, Yi, & Liya, 2016).

In addition, the vibrational constraint, which forms the main critical aspect of this study, is based on flutter speed prevention in both the working interval and stall regions, and is usually defined based on the reduced frequency as (Whitehead, 1965, 1966, 1973):

$$\lambda = \frac{bC\omega}{V_\infty} \tag{2}$$

where λ is reduced frequency, C is chord distance, ω is frequency, and V_∞ is the infinite velocity of the blade upstream. The stall flutter can be postponed based on the experimental recommendations. Indeed, the suggested empirical reduced frequency values for torsional and flexural modes should have values larger than 1.5 and 0.35, respectively (Kielb & Kaza, 1983; Lubomski, 1980; Mikolajczak et al., 1975; Smith & Yeh, 1963).

However, the main blade did not satisfy the stall flutter criteria for torsional modes, whereas the optimized blade met the reduced frequency criteria (Table 5).

Classical flutter instability is predicted by a semi-analytical in-house code based on Whitehead's theory (Whitehead, 1965, 1966, 1973). To minimize the cost of the computations, the instability condition is evaluated for a 2D section located at 75% blade length (Figure 13).
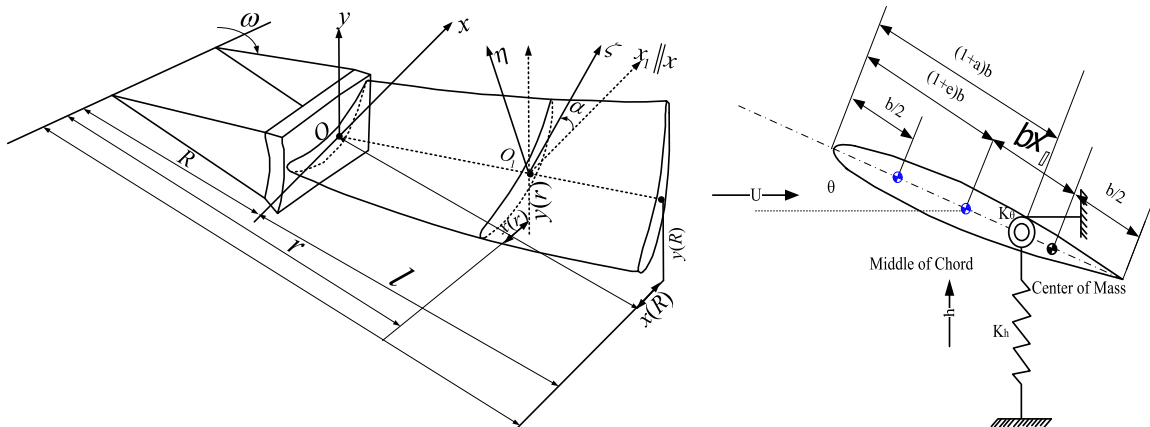

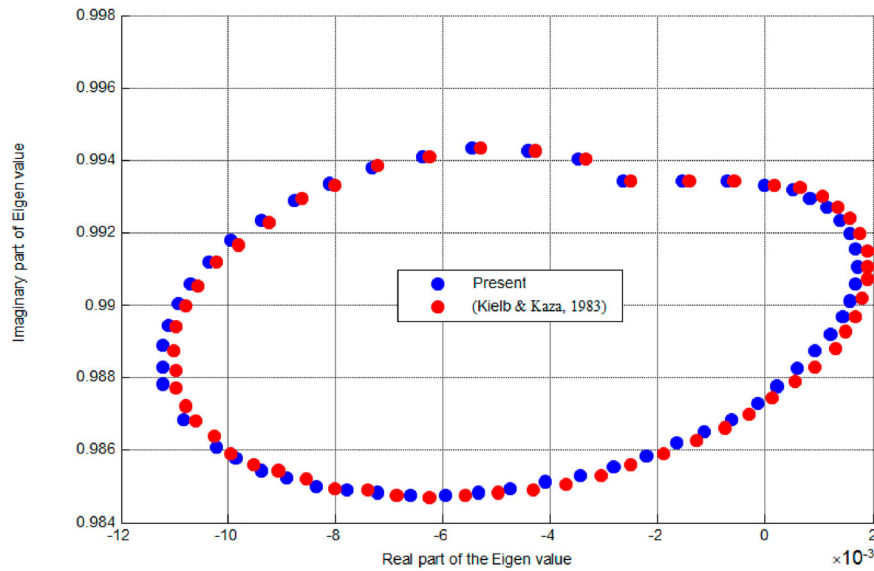**Figure 13.** Typical section of 75% airfoil.

Figure 14. Comparison of the eigenvalue part of the presented model and for $\zeta = 0$ (Kielb & Kaza, 1983).
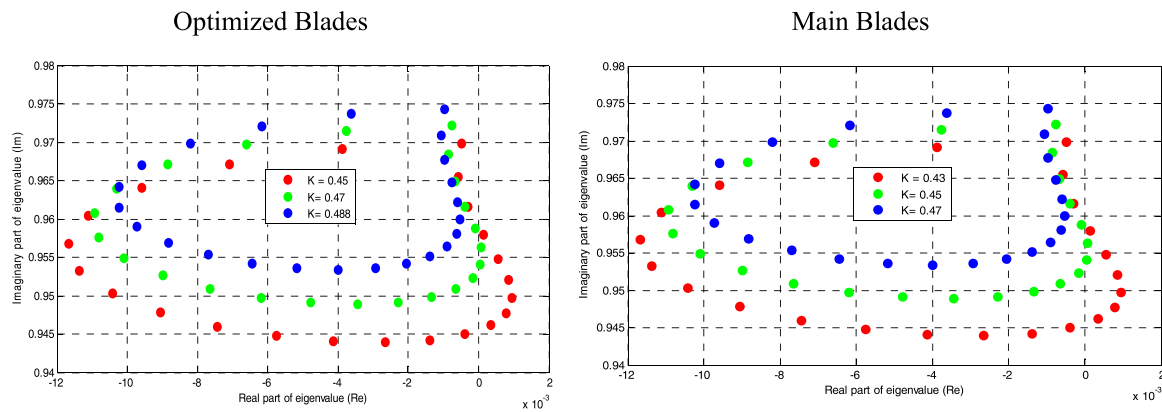

Figure 15. Comparison of main and optimized classical flutter speed estimation in three reduced frequencies.

The aeroelastic analysis is verified by a 2D typical beam, known as NASA Test Rotor 12, the parameters of which are given in Kielb and Kaza (1983). As shown in Figure 14, there is good agreement between the results of the current estimation of torsional mode in $k = 0.642$ and those predicted by Kielb and Kaza (1983).

The allowable limit of reduced frequency avoidance ($K_f = 1/\gamma$) based on the classical flutter experiments is defined in range 0.4–0.75 (Lubomski, 1980; Whitehead, 1973). Calculations show that the classical flutter speed condition in the optimized blade is improved (Figure 15).

Figure 16 illustrates the real parts of the complex conjugate form of each interblade phase angle of the blades in a row of the compressor. As shown in this figure, flutter instability happened at $k = 0.488$ reduced frequency. The results also imply that a 5.7% improvement in the torsional mode in the optimized blade (Figure 17), Table 6) is achieved (Table 7).
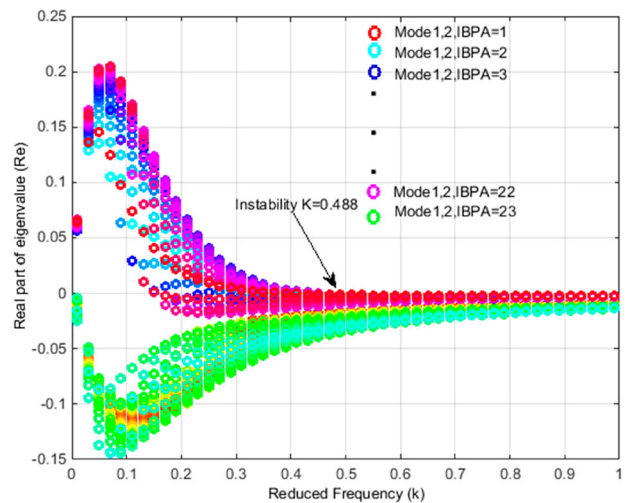

Figure 16. Variation of damping versus reduced frequency. IBPA = interblade phase angle.
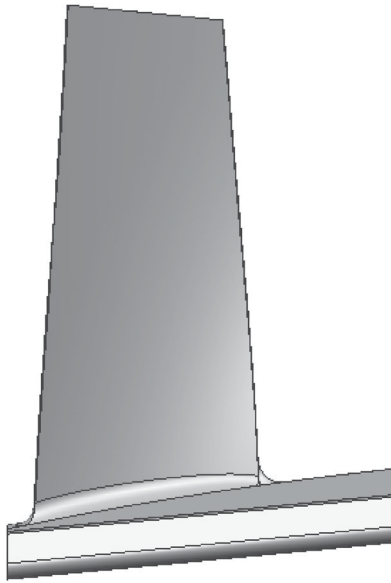
Figure 17. Optimized blade shape of the first row compressor test rig.

Table 6. Cord length and twist angle distribution of the NACA 65 airfoil along the main blade span.

Blade span (r/R)	Chord variation (%)	Dislocation of the sections (mm)
0.12	+0.1	0.13 forward
0.36	+0.11	0.3 forward
0.60	1	0.2 backward
0.84	−0.1	0.2 backward
1	−0.2	0.1 backward

Table 7. Classical flutter results.

	MATLAB code	
Stage	Torsion	
	Optimized blade	Main blade
R1	0.488	0.470

7. Conclusion

An optimization procedure based on the MDO approach in the first stages of the design of the a new compressor test rig was defined. Blade geometry was parameterized to have the best aeromechanical performance. Limitations on the stacking line position, or in other words, taper and sweep, play an important role during optimization. Using 3D simulations, the 3D shape of the optimized blade was generated. Aerodynamic performance, stress level and aeroelastic behavior of the blade were set as the aeromechanical limitations. After optimization, the results showed that the coupled behavior of the blade and aerodynamic performance improved by about 5.7% and established the best shape of the blade geometry (Figure 9). Consideration of the nonlinearity of the coupled domain in the design process and its effects on the quality of the design optimizations can be suggested for future investigations.

ORCID

Shahaboddin Shamshirband http://orcid.org/0000-0002-6605-498X

References

Ashihara, K., Goto, A., Guo, S., & Okamoto, H. (2004). *Optimization of microturbine aerodynamics using CFD, inverse design and FEM structural analysis: 1st report – compressor design.* Paper presented at the ASME Turbo eXpo 2004: Power for Land, Sea, and Air.

Demeulenaere, A., Ligout, A., & Hirsch, C. (2004). *Application of multipoint optimization to the design of turbomachinery blades.* Paper presented at the ASME Turbo Expo 2004: Power for Land, Sea, and Air.

Deng, Q., Shao, S., Fu, L., Luan, H., & Feng, Z. (2018). An integrated design and optimization approach for radial inflow turbines – Part II: Multidisciplinary optimization design. *Applied Sciences*, *8*(11), 2030.

Faizollahzadeh Ardabili, S., Najafi, B., Shamshirband, S., Minaei Bidgoli, B., Deo, R. C., & Chau, K.-W. (2018). Computational intelligence approach for modeling hydrogen production: A review. *Engineering Applications of Computational Fluid Mechanics*, *12*(1), 438–458.

Ghalandari, M., Mirzadeh Koohshahi, E., Mohamadian, F., Shamshirband, S., & Chau, K. W. (2019). Numerical simulation of nanofluid flow inside a root canal. *Engineering Applications of Computational Fluid Mechanics*, *13*(1), 254–264.

Iwaniuk, A., Wiśniowski, W., & Żółtak, J. (2016). Multidisciplinary optimisation approach for a light turboprop aircraft-engine integration and improvement. *Aircraft Engineering and Aerospace Technology: An International Journal*, *88*(2), 348–355.

Kaza, K. R. V., & Kielb, R. E. (1985). Vibration and flutter of mistuned bladed-disk assemblies. *Journal of Propulsion and Power*, *1*(5), 336–344.

Kielb, R. E., & Kaza, K. R. V. (1983). Aeroelastic characteristics of a cascade of mistuned blades in subsonic and supersonic flows. *Journal of Vibration, Acoustics, Stress, and Reliability in Design*, *105*(4), 425–433.

Lubomski, J. F. (1980). *Status of NASA full-scale engine aeroelasticity research.* NASA.

Luo, C., Song, L., Li, J., & Feng, Z. (2009). *Multiobjective optimization approach to multidisciplinary design of a three-dimensional transonic compressor blade.* Paper presented at the ASME Turbo Expo 2009: Power for Land, Sea, and Air.

Mikolajczak, A., Arnoldi, R., Snyder, L., & Stargardter, H. (1975). Advances in fan and compressor blade flutter analysis and predictions. *Journal of Aircraft*, *12*(4), 325–332.

Pathak, H., Kushari, A., & Venkatesan, C. (2008). Effects of geometric and structural parameters on coupled bending torsion flutter in turbo machinery blades. *International Journal of Turbo and Jet Engines*, 25(4), 269–282.

Shen, W., Cao, Y., & Yang, Z. (2009). Thermo-elastic-plastic analysis of coupling field and touch problem of turbine disc and blade. *Thermal Turbine*, 38, 25–28.

Smith, L. H., & Yeh, H. (1963). Sweep and dihedral effects in axial-flow turbomachinery. *Journal of Basic Engineering*, 85(3), 401–414.

Srinivasan, A. (1997). Flutter and resonant vibration characteristics of engine blades. *Journal of Engineering for Gas Turbines and Power*, 119, 742–775.

Theodorsen, T., & Mutchler, W. (1935). *General theory of aerodynamic instability and the mechanism of flutter*. NASA.

Whitehead, D. S. (1965). *Bending flutter of unstalled cascade blades at finite deflection*. Wiley Online Library.

Whitehead, D. S. (1966). Torsional flutter of unstalled cascade blades at zero deflection. R&M-3429. *British ARC*.

Whitehead, D. S. (1973). *The effect of compressibility on unstalled torsional flutter*. Wiley Online Library.

Xiaodong, Q., & Xiuli, S. (2015). Multidisciplinary design optimization of turbine disks based on ANSYS Workbench Platforms. *Procedia Engineering*, 99, 1275–1283.

Yaozeng, W., Wenxiang, W., Yi, H., & Liya, Z. (2016). API 616-2011 standard updates and its applicability to offshore platforms. *Oil & Gas Storage and Transportation*, 35(10), 1127–1131.

Zhang, M., Gou, W., Li, L., Wang, X., & Yue, Z. (2016). Multidisciplinary design and optimization of the twin-web turbine disk. *Structural and Multidisciplinary Optimization*, 53(5), 1129–1141.

Appendix

The linear form of the aerostructural equation is represented as follows (Whitehead, 1965, 1966, 1973):

$$\begin{bmatrix} m & mbx_\theta \\ mbx_\theta & I_P \end{bmatrix} \begin{Bmatrix} \ddot{h} \\ \ddot{\theta} \end{Bmatrix} + \begin{bmatrix} c_h & 0 \\ 0 & c_\theta \end{bmatrix} \begin{Bmatrix} \dot{h} \\ \dot{\theta} \end{Bmatrix} + \begin{bmatrix} k_h & 0 \\ 0 & k_\theta \end{bmatrix} \begin{Bmatrix} h \\ \theta \end{Bmatrix}$$
$$= \begin{Bmatrix} L \\ M \end{Bmatrix} \tag{3}$$

where h is the transverse displacement, θ is the torsional displacement, I_P is the mass moment of inertia, m is the mass of the system, mbx_θ is the elastic axis distance from the center of mass, c_h is flexural damping, c_θ is torsional damping, k_h is flexural stiffness, k_θ is torsional stiffness, and L and M are the lift and moment of the system, respectively. The aerodynamic formulations emerged from Theodorsen and Mutchler's (1935) unsteady theory, which is presented for a cascade model with an infinite number of blades. Small amplitude and constant phase between the blades are the main assumptions of the presented model, and the lift and moment distribution around the elastic axis is formulated as:

$$L = \pi \rho b^3 \omega^2 \sum_{r=0}^{N-1} \left[l_{hhr} \frac{h_{\theta r}}{b} + l_{h\theta r}\theta_r + l_{whr} \right] e^{i(\omega t + \beta_r s)}$$

$$M = \pi \rho b^4 \omega^2 \sum_{r=0}^{N-1} \left[l_{\theta hr} \frac{h_{\theta r}}{b} + l_{\theta\theta r}\theta_r + l_{w\theta r} \right] e^{i(\omega t + \beta_r s)} \tag{4}$$

where ρ is air density, U is infinite velocity, and the coefficients l_{whr} and $l_{w\theta r}$ are aerodynamic force functions which highlight the weak impacts of upstream flow. The other aerodynamic coefficients involving l_{hhr}, $l_{h\theta r}$, $l_{\theta hr}$, $l_{\theta\theta r}$, l_{whr} and $l_{w\theta r}$ can be introduced as:

$$l_{hhr} = \frac{2i}{k} C_{Fq}$$

$$l_{h\theta r} = \frac{2}{k^2}(C_{F\theta} - i\lambda\eta C_{Fq})$$

$$l_{\theta hr} = \frac{4i}{k}(C_{Mq} - \eta C_{Fq})$$

$$l_{\theta\theta r} = \frac{4}{k^2}(C_{M\theta} - \eta C_{F\theta} - i\lambda\eta C_{Mq} + i\lambda\eta^2 C_{Fq})$$

$$l_{whr} = \frac{-2w_r}{k^2 U}(e^{i\lambda\eta} C_{Fw})$$

$$l_{w\theta r} = \frac{-4w_r}{k^2 U}(e^{i\lambda\eta} C_{Mw} - \eta e^{i\lambda\eta} C_{Fw})$$

$$\lambda = 2k, \eta = \frac{1+a}{2}, k = \frac{bw}{U}$$

where w_r is the amplitude of the sinusoidal wake. The coefficients C_{Fq}, $C_{F\theta}$, C_{Mq}, $C_{M\theta}$, C_{Mw} and C_{Fw} are related to reduced frequency (k), interblade phase angle (β_r), pitch distance to chord ratio (s/c), damping ratio ζ of both torsional and flexural modes, and location of the elastic axis (a). Based on the sinusoidal displacement of each degree of freedom, the state space of the above equation (4) for the Sth blade can be rewritten as:

$$-\begin{bmatrix} m_s & m_s bx_{\theta_s} \\ m_s bx_{\theta_s} & I_{P_s} \end{bmatrix} \omega^2 \begin{Bmatrix} h_s \\ \theta_s \end{Bmatrix}$$
$$+ \begin{bmatrix} (1 + 2i\zeta_{h_s})m_s\omega_{h_s}^2 & 0 \\ 0 & (1 + 2i\zeta_{\theta_s})I_{P_s}\omega_{\theta_s}^2 \end{bmatrix} \begin{Bmatrix} h_s \\ \theta_s \end{Bmatrix}$$
$$= \begin{Bmatrix} \pi\rho b^3 \omega^2 \sum_{r=0}^{N-1} \left[l_{hhr} \frac{h_{\theta r}}{b} + l_{h\theta r}\theta_r + l_{whr} \right] e^{i(\omega t + \beta_r s)} \\ \pi\rho b^4 \omega^2 \sum_{r=0}^{N-1} \left[l_{\theta hr} \frac{h_{\theta r}}{b} + l_{\theta\theta r}\theta_r + l_{w\theta r} \right] e^{i(\omega t + \beta_r s)} \end{Bmatrix} \tag{5}$$

By multiplying both sides of Equation (5) into the stiffness matrix, the Equation (5) can be written in the following form:

$$-\mu_s \begin{bmatrix} \dfrac{1}{\mu_s\omega_{h_s}^2(1+2i\zeta_{h_s})} & \dfrac{x_{\theta_s}}{\mu_s\omega_{h_s}^2(1+2i\zeta_{h_s})} \\ \dfrac{x_{\theta_s}}{\mu_s r_{\theta_s}^2\omega_{\theta_s}^2(1+2i\zeta_{\theta_s})} & \dfrac{r_{\theta_s}^2}{\mu_s r_{\theta_s}^2\omega_{\theta_s}^2(1+2i\zeta_{\theta_s})} \end{bmatrix} \begin{Bmatrix} \dfrac{h_s}{b} \\ \theta_s \end{Bmatrix}$$
$$+ \frac{1}{\omega^2} \begin{bmatrix} 1 & 0 \\ 0 & 1 \end{bmatrix} \begin{Bmatrix} \dfrac{h_s}{b} \\ \theta_s \end{Bmatrix}$$
$$= \begin{Bmatrix} \sum_{r=0}^{N-1} \left[l_{hhr} \dfrac{h_{\theta r}}{b} + l_{h\theta r}\theta_r + l_{whr} \right] \dfrac{e^{i(\omega t + \beta_r s)}}{\mu_s\omega_{h_s}^2(1+2i\zeta_{h_s})} \\ \sum_{r=0}^{N-1} \left[l_{\theta hr} \dfrac{h_{\theta r}}{b} + l_{\theta\theta r}\theta_r + l_{w\theta r} \right] \dfrac{e^{i(\omega t + \beta_r s)}}{\mu_s r_{\theta_s}^2\omega_{\theta_s}^2(1+2i\zeta_{\theta_s})} \end{Bmatrix} \tag{6}$$

where

$$\mu_s = \frac{m_s}{\pi\rho b^2}, r_{\theta_s} = \frac{I_{P_s}}{m_s b^2}, x_{\theta_s} = \frac{S_{\theta s}}{m_s b}$$

Using the non-dimensional form of the following parameters, the equation of motion can be obtained as:

$$\gamma_{h_s} = \frac{\omega_{h_s}}{\omega_0}, \gamma_{\theta_s} = \frac{\omega_{\theta_s}}{\omega_0}, \gamma = \left(\frac{\omega_0}{\omega}\right)^2$$

$$-\mu_s \begin{bmatrix} \dfrac{1}{\mu_s \gamma_{h_s}^2 (1 + 2i\zeta_{h_s})} & \dfrac{x_{\theta_s}}{\mu_s \gamma_{h_s}^2 (1 + 2i\zeta_{h_s})} \\ \dfrac{x_{\theta_s}}{\mu_s r_{\theta_2}^2 \gamma_{\theta_s}^2 (1 + 2i\zeta_{\theta_s})} & \dfrac{r_{\theta_s}^2}{\mu_s r_{\theta_2}^2 \gamma_{\theta_s}^2 (1 + 2i\zeta_{\theta_s})} \end{bmatrix} \begin{Bmatrix} \dfrac{h_s}{b} \\ \theta_s \end{Bmatrix}$$

$$+ \begin{bmatrix} \gamma^2 & 0 \\ 0 & \gamma^2 \end{bmatrix} \begin{Bmatrix} \dfrac{h_s}{b} \\ \theta_s \end{Bmatrix}$$

$$= \begin{Bmatrix} \displaystyle\sum_{r=0}^{N-1} \left[l_{hhr} \dfrac{h_{\theta r}}{b} + l_{h\theta r}\theta_{\theta r} + l_{whr} \right] \dfrac{e^{i(\omega t + \beta_r s)}}{\mu_s \gamma_{h_s}^2 (1 + 2i\zeta_{h_s})} \\ \displaystyle\sum_{r=0}^{N-1} \left[l_{\theta hr} \dfrac{h_{\theta r}}{b} + l_{\theta\theta r}\theta_{\theta r} + l_{w\theta r} \right] \dfrac{e^{i(\omega t + \beta_r s)}}{\mu_s r_{\theta_2}^2 \gamma_{\theta_s}^2 (1 + 2i\zeta_{\theta_s})} \end{Bmatrix}$$

$$(7)$$

By definition of $\{X\}e^{i\omega t} = [E]\{Y\}e^{i\omega t}$, which relates the Sth mistuned blade motion to the summation of all possible interblade phase modes $\left(\begin{Bmatrix} h_s/b \\ \theta_s \end{Bmatrix} e^{i\omega t} = \sum_{r=0}^{N-1} \begin{Bmatrix} h_{ai}/b \\ \theta_{ai} \end{Bmatrix} e^{i(\omega t + \beta_r s)} \right)$, the matrix form of Equation (7) for a row of blades is obtained as:

$$([P] - [I]\gamma)\{Y\} = -[E]^{-1}[G][E]\{[AD]\} \qquad (8)$$

The stability condition of the aeroelastic system can be determined by calculation of the eigenvalue problem of the right-hand side of Equation (8). Positive values of the real part of the frequencies are specified as the flutter instability condition at different velocities.